Journal of Applied Fluid Mechanics, Vol. 18, No. 3, pp. 617-630, 2025.
Available online at www.jafmonline.net, ISSN 1735-3572, EISSN 1735-3645.
https://doi.org/10.47176/jafm.18.3.2898

Dynamic Characteristics of Near-wall Single Bubble Collapse-induced Shock Waves

W. Han[1,2], Y. Xing[1†], R. Li[1,3], W. Li[1], Y. Hao[1] and Y. Chen[1]

[1] *School of Energy and Power Engineering, Lanzhou University of Technology, No. 287 Langongping Road, Qilihe District, Lanzhou, Gansu, 730050, China*
[2] *Key Laboratory of Advanced Pumps, Valves and Fluid Control System of the Ministry of Education, Lanzhou University of Technology, No. 36 Pengjiaping Road, Qilihe District, Lanzhou, Gansu 730050, China*
[3] *Key Laboratory of Fluid Machinery and Systems of Gansu Province, No. 287, Langongping Street, Qilihe District, Lanzhou, Gansu 730050, China*

†*Corresponding Author Email: 222085802053@lut.edu.cn*

ABSTRACT

Understanding the kinetic behavior at the scale of a single bubble is crucial for understanding cavitation flow properties. In this study, experiments and numerical analysis of shock waves resulting from the crumpling of a solitary adjacent wall vacuole have been conducted. Shock wave characteristics induced by near-wall bubble collapse were investigated using high-speed photography and shadowgraphy techniques. Numerical simulations were conducted of near-wall vacuole collapse-induced shock-wave dynamics using the OpenFOAM cavitatingFoam solver. (1) The shock wave displays an essentially symmetrical distribution. The pressure maxima diminished along the sagittal diameter. The intensity of the second shock wave generated near the wall was decreased by approximately 21.2% compared to the initial shock wave. The simulated wave speeds exhibit a high level of concordance with the experimental data, and the calculated errors are below 7.9%. (2) The pressure and velocity at which the shock wave propagates in water exhibit a power function and an exponential decay function, respectively, as they travel across distance. And the perturbation profile of the velocity aligned with the direction in which the shock wave propagated. This result indicates that the shock wave acts as a catalyst for the creation of disturbances in the velocity field. (3) Constructing a transformation relation for the wave energy of near-wall vacuole collapse. During its first collapse, the near-wall cavitation bubble lost an average of 85% of its energy. This allowed for the assessment of the erosive impact of cavitation-induced shock waves on rigid surfaces.

Article History

Received June 15, 2024
Revised August 22, 2024
Accepted October 1, 2024
Available online January 1, 2025

Keywords:

Cavitation bubble
Cavitation
Pressure
Shockwave
Wave energy
High-speed photography

1. INTRODUCTION

The study of cavitation mechanisms can be traced back to Rayleigh's theory of bubble dynamics proposed in 1917. Rayleigh (1917) analyzed the behavior of a solitary bubble with a spherical shape in an ideal unbounded flow, assuming equilibrium vapor pressure within the bubble. Plesset and Prosperetti (1977) expanded upon this work by considering the effects of nonvaporizable gases, interfacial tension, and fluid fluidity. This resulted in the development of more comprehensive equations of motion pertaining to individual bubbles, than those originally proposed by Rayleigh, and Plesset and Prosperetti. Understanding the kinetic behavior at the scale of a single bubble is crucial for understanding cavitation flow properties. Recently, there has been intensive research on the dynamic properties of single bubbles (Yu et al., 2024), including high-speed jets (Zhang et al., 2016), reflected flows (Zhang, 2019), and surges (Huang, 2020).

When a vacuole collapses, it generates a shock effect on the nearby wall. There are two primary theories regarding its origin. The first is the microjet impact theory, whereas the second is the pressure-wave impact theory. Kornfeld and Suvorov (1944) first proposed the jet impact theory in their study, suggesting that the collapse of a vacuole instantaneously generates a jet with a high velocity, which they argued was the primary cause of cavitation. Conversely, the impact of pressure-wave theory is rooted in the concept of the vacuole's potential energy and can be traced back to the study by Hammitt (1963).

NOMENCLATURE

α	proportion of liquid by volume	$(\nabla U)^T$	transposed gradient of velocity field
α_v	proportion of vapor by volume	c	speed of sound
γ	distance from bubble to boundary = L/R_m	dlr	volume fraction of vacuoles
η	efficiency parameter	d/R_{max}	propagating distance
μ	viscosity	k	surface curvature
ρ	density	l	distance from center of bubble to wall
σ	surface tension coefficient	p	pressure
A	largest area of the bubble	p_{max}	peak pressure
D	strain rate tensor	p_o	original pressure within bubble = 3540 pa
E_{wave}	energy emitted by shock wave	p^*	pressure normalized by a reference value
L	initial radius from center of bubble to boundary	p_∞	ambient pressure = 1 atm
N	interfacial unit normal vector	r	distance
R_m	maximum radius	Sha	numerical shading
U	velocity tensor	t	time
U^*	velocity normalized by a reference value	t_c	time between bubble maximum and minimum volumes
∇U	gradient of velocity field	t^*	timeframe

According to this theory, the stored energy of a vacuole is associated with its volume and the pressure differential between its interior and exterior. Fortes-Patella et al. (2013) developed a near-wall impact assessment method for single vacuoles based on the potential energy of the vacuoles. They initially solved the spherical pressure wave signal released during vacuole collapse, and subsequently calculated the energy contained in the pressure wave as well as the wave-energy conversion rate. However, their method was limited to analyzing the motion of spherical vacuoles.

Optical techniques are frequently employed to study shock waves resulting from the rupture of bubbles to acquire a more profound understanding of the energy characteristics of vacuoles. Ohl et al. (1995, 1999) employed the shadowgraph method to capture and examine shockwave emissions as bubbles oscillated near a solid surface. They concluded that an initial shock wave occurs when a stream of liquid strikes the opposite boundary of the bubble and that the emergence of the second-aspect shock wave is related to the profound compression experienced by the bubble as it reaches its minimum volume. Tomita and Shima (1986) used the ripple-shadowing method to investigate this phenomenon. The researchers noted that the dynamic interaction between the bubble and the shock wave or pressure wave was crucial in creating localized areas of high pressure. This observation underscores the intricate nature of the relationship between bubble dynamics and shock wave propagation, shedding light on the underlying mechanisms governing the phenomena that lead to material damage. There have been several recent studies that focused on phenomena, such as shock waves (Lechner, et al. 2017) and return jets (Luo, et al 2018; Tagawa & Peters, 2018). However, previous research has mostly concentrated on examining the experimental (Zhang and Zhang, 2024) and computational analyses of collapses of individual bubbles near a wall. with theoretical studies on shock waves remaining insufficient.

Acoustic emissions from individual bubbles and experimental methods such as hydrophones or optical systems (Huang et al., 2024) can be used to capture shock waves, which are recognized as standard acoustic emissions during bubble evolution. Matula et al. (1998) described how shock waves had been successfully captured through a recording produced by a single bubble using a specialized hydrophone with a 10 MHz bandwidth. Brujan et al. (2008) conducted a study on the release of shock waves during a rupture. The observation of a bubble connected to an immovable surface using high-speed imaging techniques, and their results showed that shock pressure decayed as the distance from the bubble increased at a ratio of 1.5:1. Ohl et al. (1999) employed a shadowgraph approach to monitor the displacement of shock waves. highlighting that the bubble expansion was notably slower than the wave velocity. Pecha and Gompf (2000) employed a streak camera to capture visual representations of the excitation wave and achieved a better resolution for an excitation velocity of approximately 4000 m/s. Both propagation distance and energy dissipation affect the energy attenuation of spherical excitations (Lauterborn & Kurz, 2010). Supponen et al. (2017) employed a combination of simultaneous shadow mapping and hydrophone pressure measurements to see shock waves emitted during the fragmentation of an individual bubble. They also formulated a framework for forecasting the maximum shock wave pressure and energy during the implosion of an irregularly shaped bubble. Cui et al. (2018) investigated the single-bubble ice-breaking mechanism using a shadowing method and revealed that shock waves were the main cause of ice damage. Brujan and Vogel (2006) investigated the dynamic properties of cavitation bubbles in relation to the release of stress waves from water and materials resembling tissue. The material's viscoelastic-elastic characteristics were observed to cause a decrease in the period of bubble oscillation. Research has demonstrated that the impact pressure decreases as the medium exhibits heightened viscosity, an increase in elastic modulus, and plastic flow stress. Brujan et al. (2019) further investigated the dynamics of bubbles in solutions containing polymers, specifically focusing on the impact pressure generated upon bubble collapse, while scrutinizing the viscosity effect under uniaxial tensile conditions on this occurrence.

From the studies described above, two conclusions can be inferred: (1) The primary experimental techniques focus on the utilization of the shadowgraph method and hydrophones. (2) Although there has been a thorough analysis of the characteristics of shock waves, the kinetic properties of the two shock waves produced near the vacuole wall are often overlooked. Therefore, further investigation of the shock waves which are generated during the development of near-wall vacuoles is warranted. This study seeks to address the following points: (1) Explore the evolution and kinetic attributes of shockwaves at the boundary. (2) Assess energy dissipation of waves near rigid walls and determine their influence on the walls.

2. EXPERIMENTAL MATERIALS AND METHODS

Building upon previous research conducted by Chen et al. (2003) and Zhang et al. (2024), the variation across time and space of the entire liquid during the bubble-collapse process was modeled. Kinetic properties of the shock wave and energy transformation to the wall were investigated by combining experimental and numerical simulations.

2.1 Experimental Introduction

2.1.1 Bubble Generator

Figures 1(a) and 1(b) show the experimental set-up. The experiments were conducted in a square rectangular water tank measuring 800 mm in height with a base of 800 mm × 500 mm, as illustrated in Fig. 1(a). To achieve the best possible conditions for photography and lighting, the water tank was constructed using transparent acrylic panels. The tank was partially filled with water that had been degassed, and the temperature was carefully maintained at 20 °C. Bubbles were generated on the surface of the aluminum plate at the bottom of the tank using a low-voltage spark bubble generator. After conducting numerous experiments, it was determined that the maximum radius (R_m) of the bubbles fell within the range of 4±1.2 mm. To quantitatively characterize bubbles in a fluid of infinite extentthe bubble maximum radius was defined as $R_m = \sqrt{(A/\pi)}$, where A represents the largest area of the bubble. The results indicate that the initial bubble center consistently aligns with the point of contact. Hence, precise control of the initial bubble position was achieved. In this experiment, bubbles were generated along the boundary, with both ends of the boundary securely clamped with brackets and fully submerged in water. As shown in the figure, The non-dimensional distance from the bubble to the boundary is denoted as $\gamma = \frac{L}{R_m}$, where L is the initial distance from the bubble's focal point to the boundary wall. L' represents the distance between the centre of the bubble and the free surface, and we set $L' \gg R_m$. This paper does not investigate the impact of the free surface on the vacuole's collapse.**2.1.2 Shadow Method Lab Bench**

Experimental high-speed photography encompasses diffuse illumination high-speed photography and shadowing techniques. High-speed diffuse illumination is

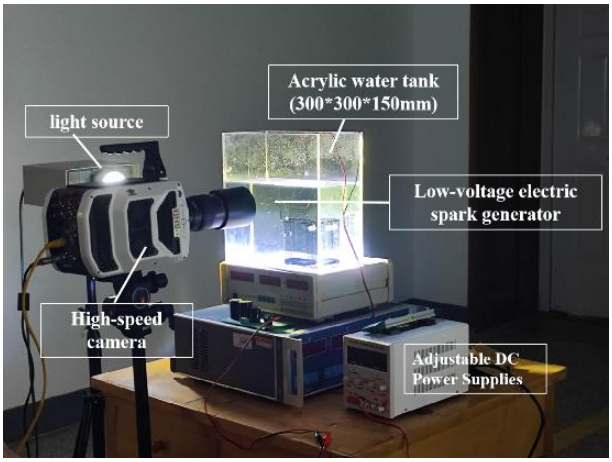

(a)

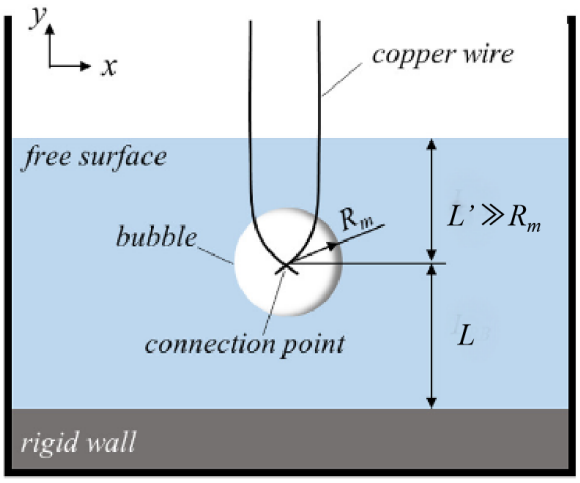

(b)

Fig. 1 Cavitation test bench

a widely adopted approach for documenting the evolution of bubbles. This method involves the use of a high-speed camera, an uninterrupted light source, and a diffusion filter. Operating at a frequency of 37,000 fps, the camera uses a 1-s exposure time. The light source, high-speed camera, and copper wire connection points are aligned along a single axis. The diffusion filter is crucial in determining the dispersion of light, thereby ensuring the effective capture of the event.

Supplementary technique: Shading was used to record the formation and spread of shock waves. This method offers higher-quality images that are more suitable than the ripple shading method for the quantitative analysis of shockwave experiments (Zhu et al., 2022). It comprises a light source, slit, convex lens, reflector, and high-speed camera. The experimental setup is illustrated in Fig. 2.

2.2 Process

This experimental approach builds on the methods outlined by Zhang et al. (2011), Ma et al. (2018), and Dular et al. (2019). Air bubbles were generated by discharging a 5500 μF capacitor assigned 60 V. The high resistance of the conductors at their closest point caused significant heat generation, resulting in the melting of the

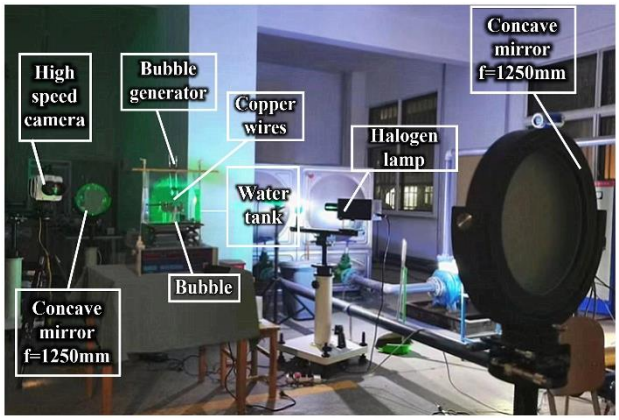

Fig. 2 Shading method lab bench

wires and the quick formation of vapor bubbles. On discharge, a copper electrode measuring 0.25 mm in diameter caused water to evaporate at the point of contact, producing extremely high temperatures and rapidly expanding bubbles, known as spark-induced bubbles. Additionally, the duration of the DC voltage discharges was very short, and the ionization time of water is negligible compared with the heat transfer time. Furthermore, shock wave formation and propagation were recorded using a high-speed camera that captured a series of heterogeneous images as parallel light travelled through a test area with a heterogeneous refractive index caused by the shock wave. A computer connected a high-speed camera to a bubble generator. As the electrical discharge machining (EDM) bubble generator was released, a high-speed camera was precisely activated to take photographs illustrating the progression of shock waves originating from the temporary bubbles.

2.3 Spatial Dimensional Calibration and Accuracy Analysis

At the onset of the capacitor discharge, the initial time was designated as $t = 0$ s. Prior to starting the experiment, a ruler was positioned along the midpoint of the initial bubble, and a picture was taken with the camera to calibrate the length. The pixels of the experimental images were then transformed using the spatial measurement values. In addition, the bubble image had an edge distortion width of 1–2 pixels, which resulted in a spatial error of 0.20–0.40 mm.

2.4 Shock Wave Capture

Shock waves are among the most destructive phenomena that occur when a vacuole collapses. As the liquid rapidly occupies the volume of the vacuole, the gases contained within the bubble experience intense compression from the surrounding liquid, creating a highly transient region of elevated pressure where a shock wave is generated. This is due to the sudden release of molecules and atoms into the medium following compression. Subsequently, the medium returns to its initial state, releasing compressed energy. Thus, the formation of shock waves is intricately linked to the compression and release processes of the medium, as depicted in the images in the second row of Fig. 3 (t = 0–77.24 ms).

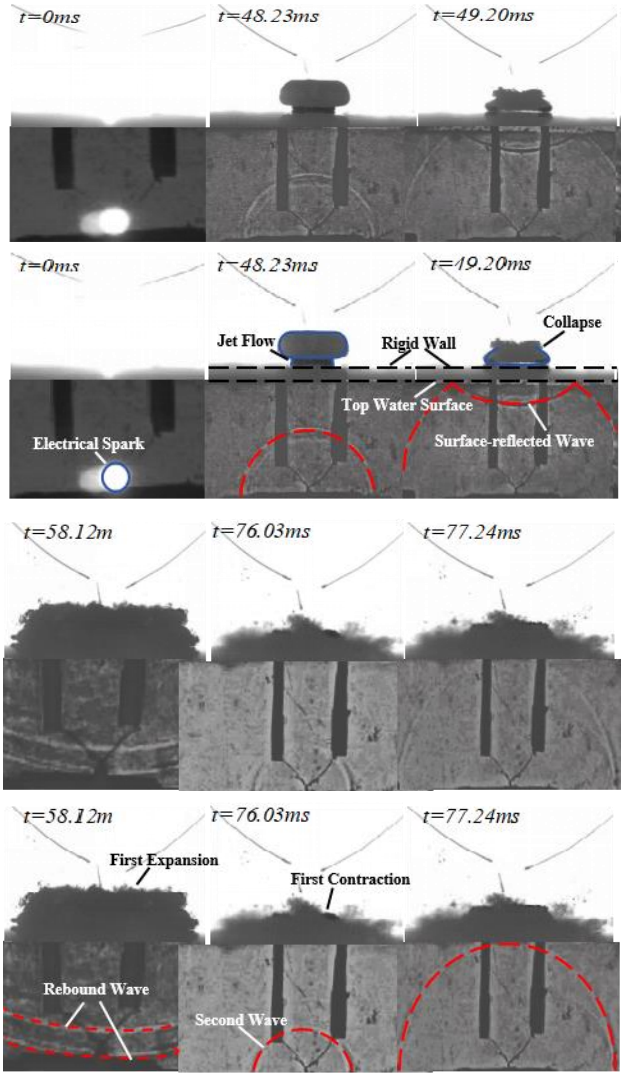

Fig. 3 Near-wall single vacuole collapse and corresponding shock wave images

In the first row, at t = 48.23 ms, when the vacuole made contact with the solid surface and rapidly collapsed, high-speed flow and pressure changes occurred, pushing the neighboring liquids towards the solid surface, forming a liquid columnar flow. The first shock wave was emitted, causing a sudden density change in the fluid, which inevitably altered the optical properties of the flow. Concurrently, the columnar flow rapidly expanded outward during the vacuole collapse to create a collapsed annular liquid column. Owing to the inertia and surface tension, this liquid column swiftly collided with the surrounding liquid and wall at t = 76.03 ms, resulting in the emergence of the second shock wave. Nevertheless, judging from the shaded graph, it is evident that the second shock wave was significantly weaker when compared with the first.

Furthermore, the shock waves also generated vibrations in the walls belonging to the water tank, resulting in the production of additional sound waves. As these sound waves travelled through the water tank, they experienced multiple instances of reflection and bouncing off surfaces within the medium, resulting in the distortion of

background images, as illustrated in the fourth image of the second row.

Therefore, from an experimental perspective, the near-wall bubble collapse caused a second shock wave. primarily associated with the interaction between the liquid and solid surfaces and the complexity of the dynamic behavior of the liquid during the collapse process.

Figure 3 depicts the images of near-wall single bubble collapse, corresponding to generation of two shock waves when $\gamma = 2$.

3. NUMERICAL SIMULATION

3.1 Numerical Methods and Platforms

Discretization was performed on the OpenFOAM platform, using a multiphase flow solver called cavitatingFoam. The control equations were discretized using the finite volume method. Time derivatives were handled in an implicit Euler format. For the gradient terms, a body-centered to face-centered interpolation was applied using the default Gaussian integral with a center-difference format. The convection terms were linearly interpolated using Gaussian integrals. A uniform orthogonal mesh was used for computational stability, eliminating the need for an orthogonal correction. The Laplace terms involve surface normal gradients computed using a non-orthogonal correction of Gaussian integrals. For the coupled pressure-velocity problem, the PIMPLE algorithm iteratively finds a solution. The residuals were adjusted to a value of $1e^{-6}$ to guarantee a precise calculation accuracy.

3.2 Research Object

This study specifically examined the production of shock waves resulting from the implosion of a solitary vacuole at a short distance from the wall surface. The initial maximum radius was defined as $R_m = 4$ mm, while the undefined distance from the vacuole to the boundary was set at different values of γ (1, 1.5, 2, 2.5, and 4). Several assumptions were made: the bubble exhibited spherical symmetry; the liquid around it was infinitely compressible and viscous; compressibility and viscosity showed a minimal correlation; gravity and diffusion had a completely insignificant impact; within the bubble, the pressure remained uniform; and the gas that could not be condensed was nonviscous. Additional assumptions were that the gas and liquid would maintain their physical properties, and that heat conduction would be neglected along with thermal effects.

3.3 Kinetic Equations for Bubble Collapse

We approached the fluid as a homogeneous two-phase mixture containing bubbles, describing the interfacial behavior between different liquid or gas phases. This also accounts for the viscosity, surface tension, and compressibility of the fluid. The governing equations are as follows.

$$\frac{d\rho}{dt} + \rho\nabla \cdot \mathbf{U} = 0, \tag{1}$$

$$\rho\frac{\partial \mathbf{U}}{\partial t} + \rho\mathbf{U} \cdot \nabla\mathbf{U} = \rho\mathbf{g} - \nabla p + 2\nabla \cdot (\mu\mathbf{D}) - \frac{2}{3}\nabla(\mu\nabla \cdot \mathbf{U}) + \sigma\kappa\mathbf{N}, \tag{2}$$

$$\frac{d\alpha}{dt} = \frac{\partial\alpha}{\partial t} + \mathbf{U} \cdot \nabla\alpha = 0, \tag{3}$$

$\mathbf{U}$ is the velocity; p is the pressure; $\mathbf{D}$ is the strain rate tensor, which is calculated as the average of the gradient of the velocity field ($\nabla\mathbf{U}$) and its transpose $(\nabla\mathbf{U})^T$, divided by 2; k is used to indicate the surface curvature; σ is the surface tension coefficient; $\mathbf{N}$ is the interfacial unit normal vector; α is the liquid volume proportion;. and ρ and μ are the density and viscosity of the mixture, respectively, which were multiplied by the corresponding volume fractions to obtain weighted values:

$$\rho = \alpha\rho_1 + (1-\alpha)\rho_2, \tag{4}$$

$$\mu = \alpha\mu_1 + (1-\alpha)\mu_2, \tag{5}$$

The subscript symbols 1 and 2 differentiate between the liquid (water) and gas (vapor) states, respectively. The Rayleigh-Ples equation (Rayleigh, 1917) is simplified by assuming that the pressure in the bubble remains constant during the modeling of spherical bubble motion. Based on this assumption, the vapor pressure was set to a constant value. In Eq. (4), ρ_1 is the density of the liquid phase and ρ_2 is the density of the vapor phase, which can be expressed as, respectively:

$$\rho_1 = \rho_{10} + \frac{1}{c_1^2}p \tag{6}$$

$$\rho_2 = \rho_{20} + \frac{p}{c_2^2} \tag{7}$$

where ρ_{10} and ρ_{20} are the density constants, and c_l and c_2 are the velocity of sound in the liquid and vapor, respectively. Setting ρ_{10} = 998 kg/m^3 , ρ_{20} = 0, c_l = 1500 m/s, c_2 is given by calculations under the isentropic flow assumption.

The Reynolds number is defined as:

$$Re = \frac{\rho v d}{\mu_m} \tag{8}$$

where v is the mean fluid velocity and d is the characteristic length. In this study, the maximum mean velocity reached in the whole flow field is $v = 8.6 \times 10^{-3}$m/s, and the characteristic length is d = 0.05 m, $\mu_m = 1.01 \times 10^{-3}$ Pa·s. The obtained Reynolds number is Re= 426. According to the critical Reynolds number Re_c = 2320 and μ_t= 0 in engineering applications, this study is laminar flow.

3.4 Boundary and Initial Conditions

The boundary types include 'empty,' ‘patch,’ and ‘wall.’ ’Empty’ defines a region that does not affect the flow field and is essentially a blank area in the simulation domain where conditions like velocity or pressure are not necessary. 'Patch,' is used for defining general regions not necessarily corresponding to actual object surfaces, and is typically used for defining inlet and outlet surfaces or symmetry surfaces within the calculation domain where conditions such as velocity and pressure need to be set. 'Wall,' is used to define object surfaces or boundaries where interactions between the fluid and the object occur, requiring the setting of boundary conditions such as

Table 1 Boundary condition settings in the near-wall region

Boundary name	Boundary type	Volumetric fraction α_v
Top	Patch	Uniform 0
Bottom	Wall	Uniform 0
Left	Wall	Uniform 0
Right	Wall	Uniform 0
Front & back	Empty	Empty
U	**P**	**ρ**
Zero Gradient	Total Pressure	Fixed Value
Uniform (0 0 0)	Uniform ($1e^5$)	Uniform (1000)
No Slip	Zero Gradient	Zero Gradient
Zero Gradient	Total Pressure	Fixed Value
Uniform (0 0 0)	Uniform ($1e^5$)	Uniform (1000)
Zero Gradient	Total Pressure	Fixed Value
Uniform (0 0 0)	Uniform ($1e^5$)	Uniform 1000
Empty	Empty	Empty

velocity, pressure, and density. Table 1 shows the conditions and boundaries used.

The symbol α_v in the table represents the proportion of vapor volume. The volume fraction of the gas phase at the boundary is uniformly distributed and set to zero. Therefore, the boundary was completely composed of water at the beginning of the computational domain. In the velocity field U, the term "zero gradient" indicates that the gradient of velocity at the boundary is zero, and that there is no change in velocity along the normal direction. "Uniform (0 0 0)" indicates that the initial velocity values at this boundary are zero. This boundary condition is typically used to describe the interface between a fluid and stationary object, ensuring that the fluid does not cross the boundary. The bottom velocity boundary is set as a no-slip wall. "Total Pressure" represents the pressure considered as total pressure, which, in this context, corresponds to the static pressure of the external environment. "Uniform $1e^5$" denotes the numerical value of the total pressure, while in "Fixed Value," "Uniform (1000)" represents the density set to a fixed value of 1000 kg/m³. The density at the bottom near the wall is adjusted to "zero gradient" to consider the impact of the wall on the fluid.

3.5 Mesh-Independent Verification

Based on the computational model shown in Fig. 4, seven sets of grids were generated and a grid-independence test was conducted for each set, as illustrated in Fig. 5. The pressure change during the collapse of the vacuole at the monitoring point is shown in Fig. 6. This study focused on a vacuole with an initial radius of 1 mm, and a numerical simulation of the collapse process was performed. A monitoring point was set at the center of the bubble that showed a progressive increase in both the time required for the bubble to collapse and the highest velocity of the jet. Upon reaching a total grid count of 1×10^6, numerical simulation converged sufficiently. For a comprehensive

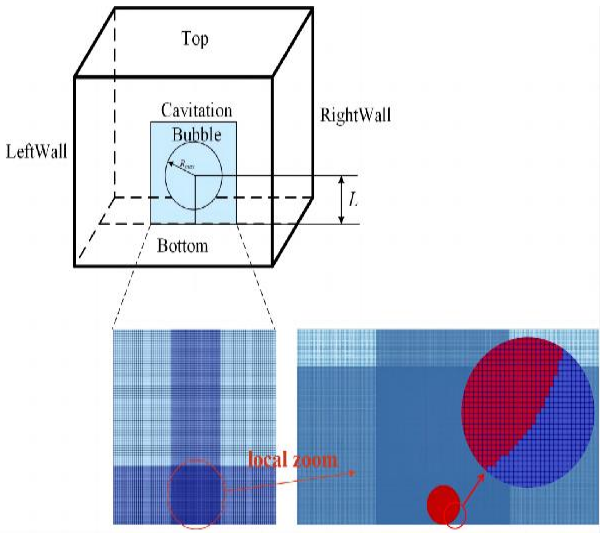

Fig. 4 Computational domain model and mesh encryption

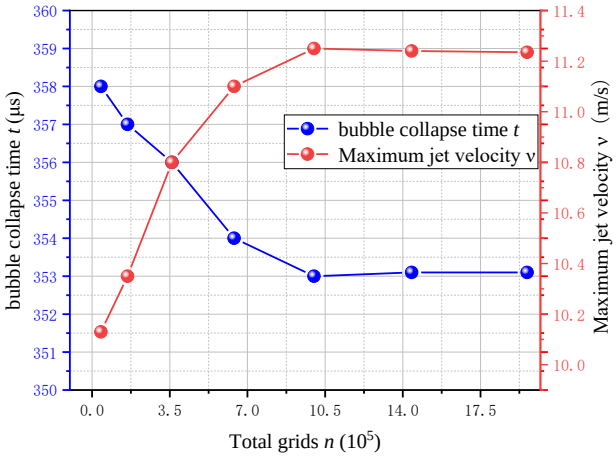

Fig. 5 Variation of parameters with total number of grids at monitoring points

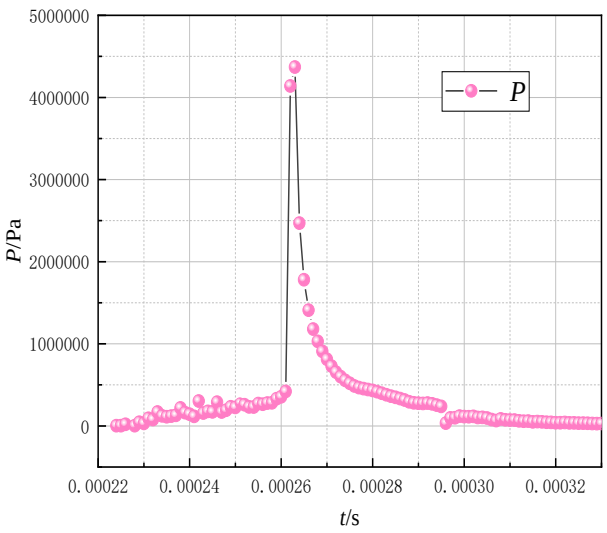

Fig. 6 Pressure changes at monitoring point

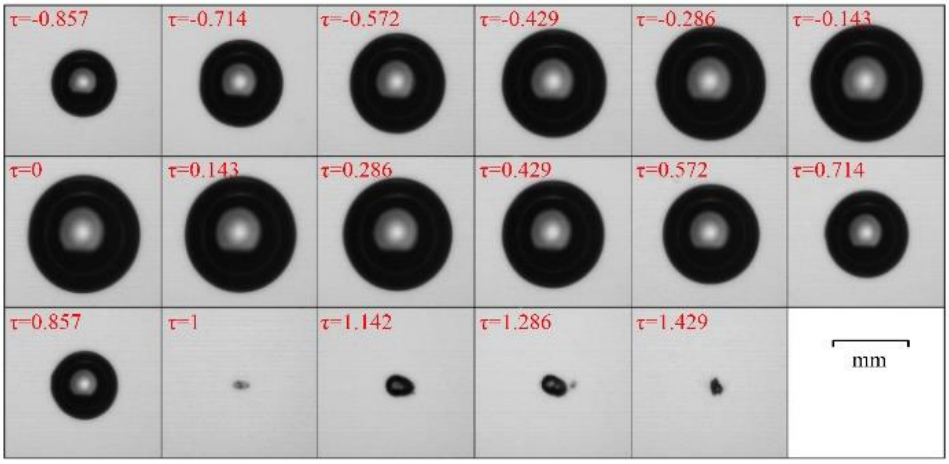

Fig. 7 Morphological evolution of free domain bubbles (starting 10 μs after the formation of the vacuole), at intervals of 10 μs. R_{max} is approximately 750 μm

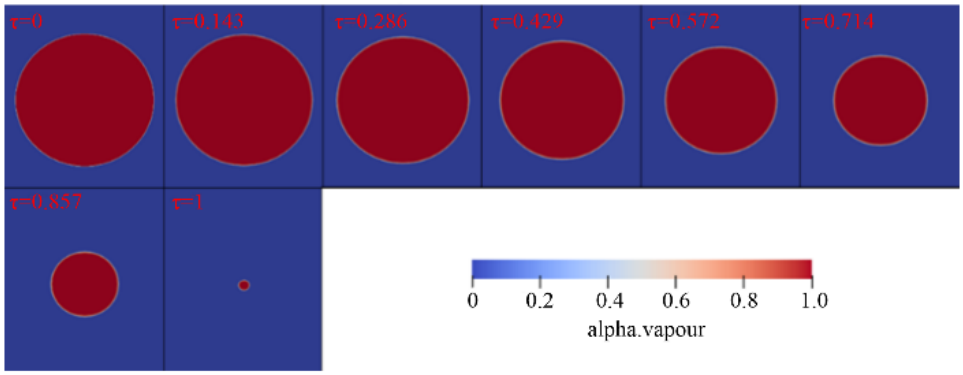

Fig. 8 Free-domain numerical simulation of bubble morphology evolution (R_{max} = 1000 μm)

analysis using mesh delineation with a total grid count of 1000 × 1000, the encrypted area encompassed 700,000 grids. The corresponding number of nodes with 1 mm vacuole radius is 36.

3.6 Reliability Verification of Numerical Simulation Methods

Figure 7 shows that the experimentally obtained complete laser-induced evolution of the vacuole from the minimum radius to the maximum radius and then collapse and rebound, to be consistent with the numerical simulation in the dimensionless time; τ = 0 was set at the maximum volume of the vacuole, and the minus sign in the figure indicates that the vacuole was in the expansion stage. The cavitation's evolution in the numerical simulation is displayed in Fig. 8. The cavitation results prior to collapse as predicted by numerical simulation exhibit full congruence with the theoretical and experimental values, and the assumption is made that the cavitation collapses from the maximum radius during the numerical simulation.

So far, the process of cavitation collapse has been analyzed using experimental and numerical simulation methods. The maximum pressure generated by the cavitation collapse in the free domain is 45.5MPa. The numerical simulation employs the compressible finite volume method to calculate the evolutionary collapse

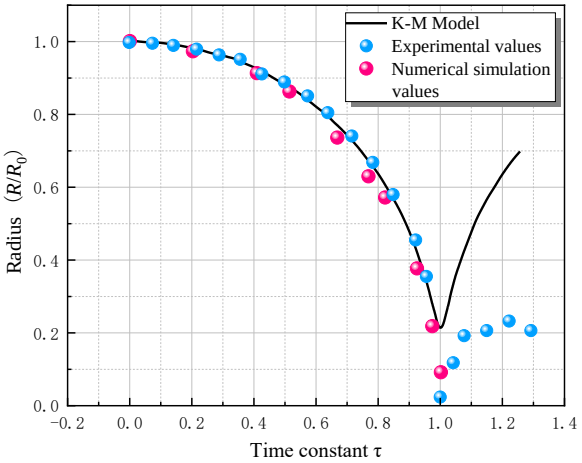

Fig. 9 Changes of cavity radius with time

process of a single cavity. The numerical model used is more complex than the K-M model and accounts for phase changes during bubble collapse. In contrast, the K-M model typically doesn't consider phase changes, which explains the differences between the observed minimum radius in Fig. 9 and the K-M predictions. Our simulations didn't include bubble rebound and focused on the first

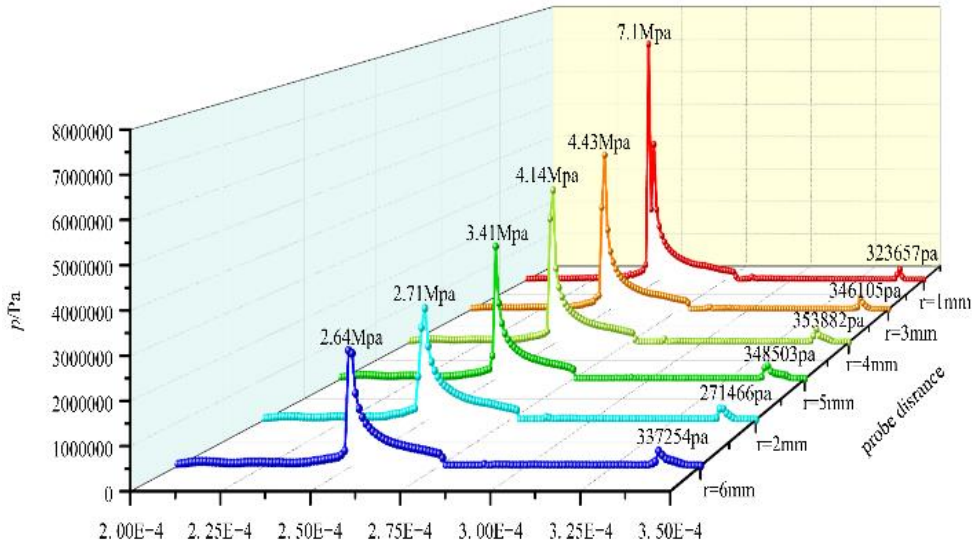

Fig. 10 Radial distribution of pressure at different observation points (R_m = 1 mm, γ = 2) _

oscillation. The simulation results closely match theoretical and experimental values before collapse, demonstrating that the cavitating Foam solver accurately models the bubble collapse process, providing strong support for future simulations of bubble collapse near surfaces.

4. RESULTS AND DISCUSSION

4.1 Shock Wave Pressure and Velocity Characteristics

To study the propagation of waves in space, first, the radial distribution of pressure at different monitoring points was investigated at $\gamma = 2$ and the results are shown in Fig. 10. The center of the bubble was then taken as the origin, and six observation points were set up at equal intervals of 1 mm from the radius position to monitor the pressure wave propagation. Figure 10 shows two distinct pressure peaks occurring at the center of the bubble, at each observation point, the existence of two pressure peaks was also found previously by Trummler et al. (2021) and Goncalves da Silva et al. (2021); the second peak was much smaller than the first and appears 70–75 μs after the first pressure peak. The numerical simulation also proves the second wave's existence. In this process, the bubble first generates a significant pressure peak during its initial collapse. Subsequently, the bubble rebounds due to gas compression and surface tension, and the near-wall effects further amplify the pressure fluctuations caused by this rebound, leading to the occurrence of a second pressure peak.

The wave propagation speed can then be estimated by measuring the distance between two neighboring peaks, as shown in Fig. 11: When the wave propagates from r = 4.09 mm at 249 μs to r = 10.44 mm at 253 μs, the propagation velocity is 1587.5 m/s, which is roughly equivalent to the speed of sound in Eq. (6) (1500 m/s). Comparisons of the two datasets derived from a numerical simulation of the wave propagation velocity and experimental measurement of the wave propagation speed is shown in Fig. 12.

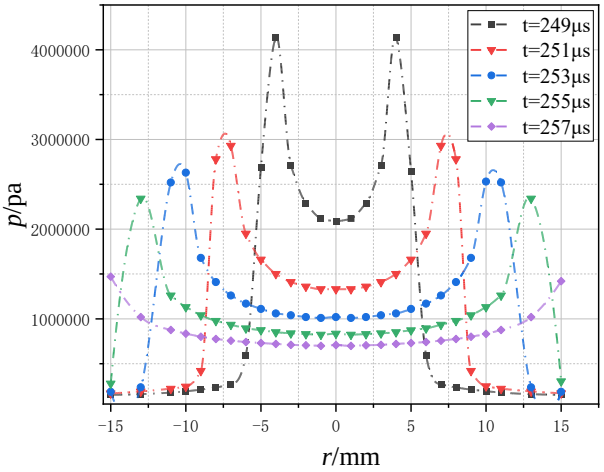

Fig. 11 Variation of shock wave pressure along the vectorial diameter of the bubble (γ = 2)

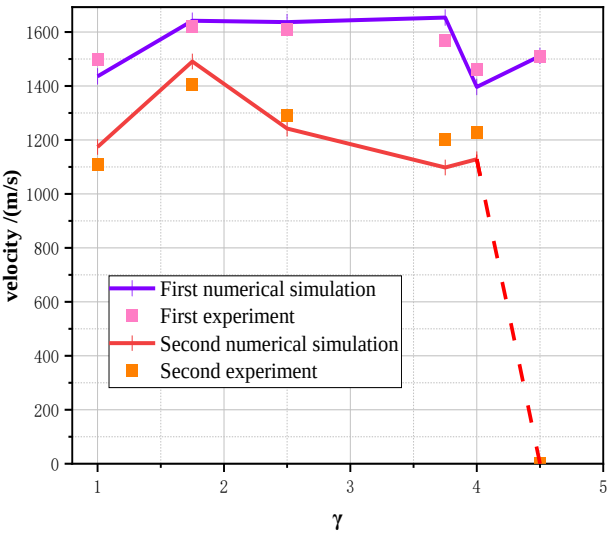

Fig. 12 Shock wave speeds for experimental measurements and numerical simulations

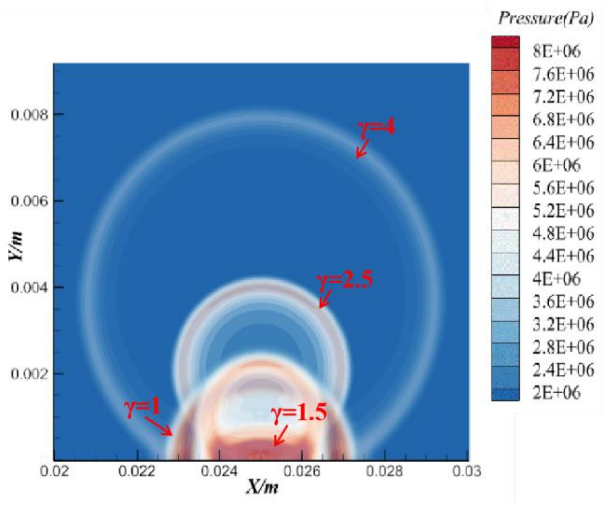

Fig. 13 Combining bubble center pressures at different distances from the wall

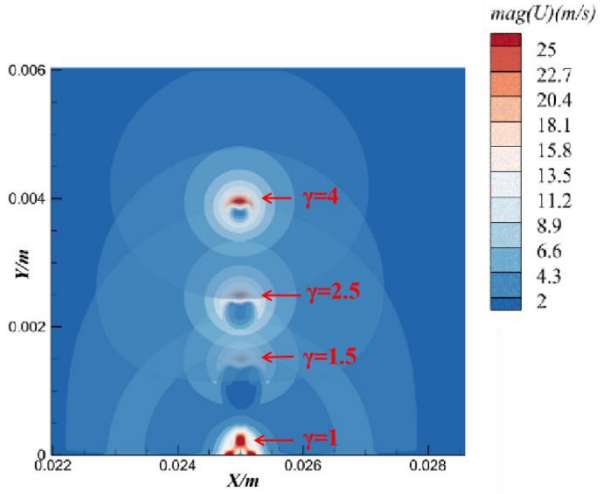

Fig. 14 Combining bubble center velocities at different distances from the wall

Experiments using the shock wave front at different positions were conducted, and the absolute speed of the shock wave propagation and change rule were calculated. The experimentally measured shock wave speed and numerical simulation results were approximately the same, with a calculated maximum error of 7.9%, which is acceptable. The second shockwave velocity was weaker than the first. Analysis of the three graphs shows that the wave passed through the monitoring points successively according to the distance, and the wave showed an approximately symmetrical distribution. As the pressure wave moved away from its origin, the maximum value decreased, illustrating the typical features of spherical waves. The second shock wave weakened by an average of approximately 21.2% in order of magnitude relative to the first shock wave.

Figures 13 and 14 illustrate the first pressure and velocity fluctuation cloud diagrams resulting from vacuole collapse at different distances from the wall (γ=1, 1.5, 2.5, and 4). Numerical simulations visually verified the effects of shockwave pressures and velocities at different wall surfaces from the core of the bubble, whose radius is the same as that on the wall surfaces to varying degrees. The shock pressure is highest at $\gamma = 1.5$, reaching 7.6 MPa, followed by $\gamma = 1$ at 4 MPa, with gradual pressure reduction beyond $\gamma = 2.5$. Regarding velocity, it peaks at $\gamma = 1$, then $\gamma = 4$, with minor disparity between $\gamma = 1.5$ and $\gamma = 2.5$.

To gain a deeper understanding of how the near-wall shock wave is formed, the numerical results provide a detailed description of how both the near-wall void and shock wave evolve over time. Figure 15 depicts the temporal evolution of the shockwave velocity and pressure, as determined from the computational results. The timeframe is denoted as a non-causal period $t^* = t/t_C$, in which the variable quantity t_C represents the duration between the bubble's maximum and minimum volumes. The ribbon bars in Fig. 11, arranged in a left-to-right manner, represent the volume fraction of vacuoles (*dlr*), velocity normalized by a reference value (U^*), numerical shading (*Sha*), and pressure normalized by a reference value (p^*). The velocity and pressure are normalized by defining them as

$$p^* = p/\rho_l c^2 \tag{8}$$

$$U^* = \sqrt{u_x^2 + u_y^2}/c \tag{9}$$

where ρ_l represents the water's density, whereas u_x and u_y represent the horizontal as well as vertical components of velocity, respectively.

When t/t_C is between 0.91 and 1.00, the volume of the vacuole is compressed to its smallest size, resulting in the generation of jets and shock waves. The shock wave formation can be distinctly observed by the white contour rings of *sha* in Fig. 15. Vacuole maintains a high internal pressure of 7.17 MPa. At a pressure of 4.7 MPa and a time ratio of $t/t_C = 1$, a shock wave was generated, resulted in an outward radiation of high pressure, as depicted in the pressure contour plot in Fig. 15(b). The first vacuolar jet can be observed in the *dlr* plot. The vacuole then proceeds to expand and rebound at a time ratio of $t/t_C = 1.08$ after the jet is generated near the wall. As vacuole expansion decelerates, the surrounding velocity also decreases. Nevertheless, the perturbed area of the speed field continues to expand. The *sha* profile exhibits distinct and easily observable bright rings that are identified as shock waves. The pressures surrounding bubble decrease as they expand.

The bubble undergoes expansion during $t/t_C = 1.04$–1.08, the numerical simulation plot clearly shows two white contours, which are two shock waves formed due to the reflection from the wall. The alignment of the velocity disturbance patterns with the direction of shock wave propagation suggests that perturbations in the velocity field are most likely triggered by shock waves. Following the shock waves, the velocity of the flow field intensified, aligning with Euler's equation and the principle of mass conservation in fluid dynamics. The findings indicate that as the wave propagation distance increases, both the pressure generated by the shock wave. At the same time, its impact on the fluid velocity decrease. The relationship between the peak pressure P_{max} and propagating distance d/R_{max} is expressed by a power-function fitting:

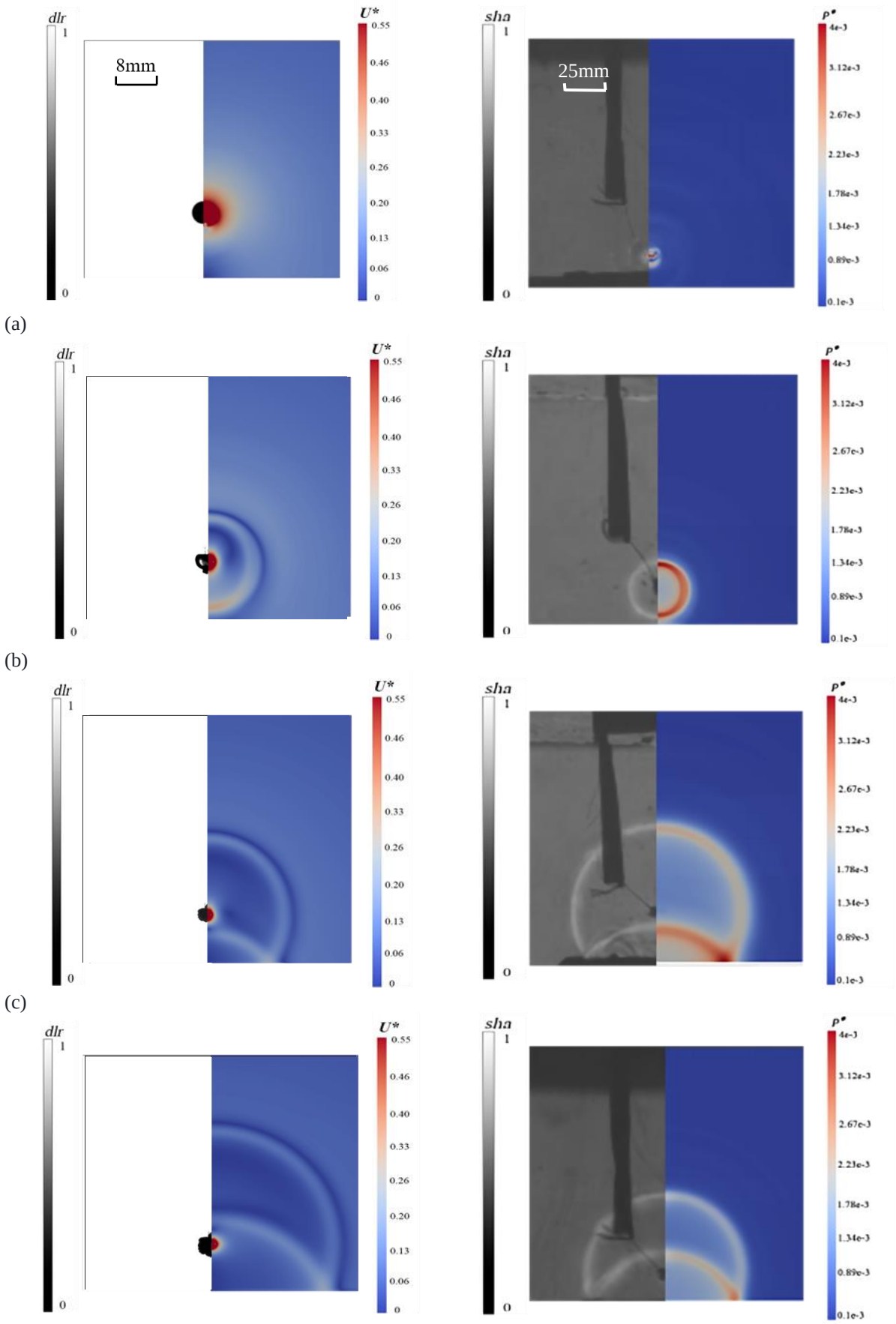

Fig. 15 Time evolution of the shock wave, including contours of the gas-liquid integration number (*dlr*), normalized velocity (*U), numerical shading (*sha*) and normalized pressure (*p**): (a) t/t_c = 0.91; (b) t/t_c = 1.00; (c) t/t_c = 1.04; (d) t/t_c = 1.08**

$$P(d/R_{max}) = \frac{1.28\times10^7}{(1+13800\cdot d/R_{max})^{0.64}} \quad (10)$$

The correlation between shock wave velocity and propagation distance is expressed by fitting an exponential decay function as follows:

$$v(d) = 1590.6 \cdot e^{-168.35\cdot d} \quad (11)$$

4.2 Energy Transfer from Pressure Waves to Solid

4.2.1 Mathematical Modelling

The initial energy of the vacuole can be derived using the spherical collapse equation developed by Rayleigh (1917).

$$E_{B0} = \frac{4}{3}\pi(p_\infty - p_0)l^3 \quad (12)$$

where, p_∞ is the ambient pressure, = 1 atm (101.3 Kpa), p_0 stands for the original pressure within the bubble, taken as 3540 pa, and the variable l represents the distance between the central point of the bubble and the wall.

A wave is defined by its emitted energy E_{wave}, and the pressure wave is calculated using the acoustic energy method (Vogel et al., 1989; Fortes-Patella et al., 2013). The energy of the spherical sonic transient is then determined as:

$$E_{wave} = \frac{4\pi l^2}{\rho c}\int p^2 dt \quad (13)$$

Based on the experimental and simulation results, it can be inferred that the dimensionless pressure wave shape remained consistent and independent of the initial conditions of the bubble. Thus, vacuolar features have an impact on both parameters of the wave, namely, p and dt.

The pressure wave signal generated by the vacuole's collapse can be characterized by the two parameters: P_{max} and σ, which is the surface tension coefficient and effectively represents the time it takes for the wave to pass through the crest. The Gaussian pulse function (Chen et al., 2020) can express the wave image well as shown in the following equation. The time to pass through the wave crest is given by the width of the pressure signal at $p = p_{max}/2$, as shown in Fig. 16 below.

$$f(t) = A \cdot \exp\left(-\frac{(t-t_c)^2}{2\sigma^2}\right) \quad (14)$$

Where A is the amplitude, t_c is the moment corresponding to the amplitude, and σ represents half of the pulse width. Where t_c determines the center of the curve and σ determines the width of the curve.

Substituting Eq. (14) into Eq. (13), with t taken from 0 to +∞, we estimate the amount of energy released as the wave travels from the focal point of the bubble towards the solid wall and obtain:

$$E_{wave} = \frac{2\sigma\pi^{\frac{3}{2}}l^2P_{max}^2}{\rho c} \quad (15)$$

When a wave collides with an immobile surface at a fixed location, the peak pressure applied to the solid wall (P_{max}) is a measure of the peak pressure. The transmission coefficient of the incident wave to the high-impedance material can be assumed to be 2; therefore, $P_{max} = \frac{1}{2}P_{solid}$ was used here.

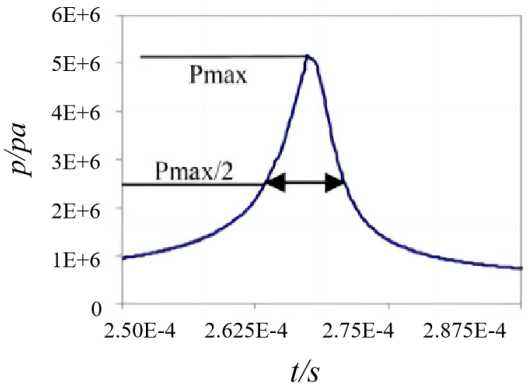

Fig. 16 Time distribution of pressure signal at r = 1 mm in the center of the bubble

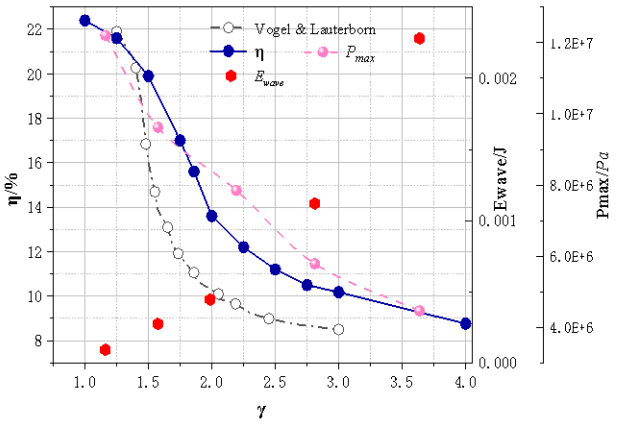

Fig. 17 Wave energy loss for different near-wall distances

Therefore, to estimate the effect of wave energy on the wall in the near-wall case from the energy balance point of view, the efficiency parameter η, defined as the ratio of the wall pressure wave energy to the initial potential energy E_{BO}, is introduced to derive the energy destruction rate of the wave on the wall:

$$\eta = 1 - \frac{E_{wave}}{E_{BO}} \quad (16)$$

4.2.2 Energy Transformation of the Collapse

To validate the precision of the model, we compared the results obtained from an experiment conducted by Vogel and Lauterborn (1988), as shown in Fig. 17. The purpose of comparison with the experiment was to verify the accuracy of the model.

The energy conversion at $1.0 \le \gamma \le 4.0$ was studied, and the conversion of the shock wave energy loss was particularly pronounced in the range of $1.3 \le \gamma \le 2.6$, with an average energy loss of 85% for near-wall cavitation bubbles during the first collapse. It has been proposed that acoustic emission is the most dominant damping mechanism for spherical cavitation bubbles collapsing in water, with up to 90% and an average of 73% of the energy loss due to emission from acoustic transients. Heat

conduction and fluid thickness have negligible effects on reducing the vibrations of the temporary round bubbles. These results align well with the theoretical research of Vogel et al. (1989), Fujikawa and Akamatsu (1980), and others as well as with the experimental work of Teslenko (1980). It contributes no more than 10% to the energy depletion of the vacuole within the specified range $1.3 \leq \gamma \leq 2.6$, when most of the energy is due to wave propagation.

Hence, the suggested streamlined mathematical model is able to be utilized to analyze the dynamics of vacuoles and forecast the potential impact of vacuole collapse on walls by assessing the E_{wave} / E_{B0}. Wave dynamics characteristics, such as the amplitude, wave passage time, and energy of the emitted pressure wave, were estimated.

5. CONCLUSION

An experimental apparatus based on the shadow method was set up to investigate the shock wave under the influence of the wall surface during the development and collapse of an EDM-induced bubble. The accuracy of the experiments was verified by a numerical simulation of the compressible finite volume method with the OpenFOAM software cavitatingFoam solver to analyse the shock wave kinematics in more depth.

(1) The shadowgraph images illustrated the formation and propagation of the shock waves, and the energy release from the collapse of bubbles due to radiation was clearly visible

(2) Two shock waves are generated when $\gamma < 4.5$, with the second shock wave weakened by approximately 21.2% relative to the first. The waves exhibit an approximately symmetrical distribution. Quantifying the correlation and confirming that the peak decreases as the pressure wave moves away from the center point, shows the typical characteristics of spherical waves. The results obtained from the experiments and numerical simulations are approximately the same.

(3) The experimental and numerical simulation results demonstrated that as the propagation distance increased, the intensity of the shock wave and its influence on the velocity of the liquid diminished. A power function and exponential decay function were used to express their relationships. The perturbation profile of the velocity aligned with the direction in which the shock wave propagated. This result indicates that the shock wave acts as a catalyst for the creation of disturbances in the velocity field.

(4) A mathematical model for the near-wall wave energy was introduced, resulting in an average energy loss of 85% near the wall. In addition, during the entire vacuole collapse process, an average energy loss of 73% was attributed to the emission of acoustic transients. Within the interval of $1.3 \leq \gamma \leq 2.6$, it exerts a contribution of less than 10% to the energy dissipation of the vacuole.

ACKNOWLEDGEMENTS

This work was supported by the Key Laboratory of Fluid Machinery and Systems of Gansu Province, the National Natural Science Foundation of China (52179086,52269022), the Natural Science Foundation of Gansu Province (23JRRA788), and in part by the Key Technology Research of Large-Scale Stepped Pumping Station Renovation of Jingtai River Electricity Irrigation Project (2020-70).

CONFLICT OF INTEREST

The authors have no conflicts to disclose.

AUTHORS CONTRIBUTION

Yifan Xing: Conceptualization, Software, Data curation. **Wei Han:** Data curation. **Rennian Li:** Funding acquisition; investigation. **Wangxu Li:** Investigation. **Yucheng Chen:** Investigation. **Yingjian Hao:** Investigation.

REFERENCES

Brujan, E. A., & Vogel, A. (2006). Stress wave emission and cavitation bubble dynamics by nanosecond optical breakdown in a tissue phantom. *Journal of Fluid Mechanics, 558*, 281–308. https://doi.org/10.1017/S0022112006000115.

Brujan, W. A., Ikeda, T., & Matsumoto, Y. (2008). On the pressure of cavitation bubbles. *Experimental Thermal and Fluid Science, 32(5)*, 1188–1191. https://doi.org/10.1016/j.expthermflusci.2008.01.006.

Chen, N., Yan, B., Li, Z. J., Li, L., & He, N. (2020). Research on laser etching of CVD diamond based on Gaussian pulse. *China Laser, 47(12)*, 127-134. http://doi.org/10.3788/CJL202047.1202007.

Chen, X., Bian, B. M., Shen, Z. H., Lu, J., & Ni, X. W. (2003). Equations of laser-induced plasma shock wave motion in air. *Microwave and Optical Technology Letters, 38(1)*, 75–79. https://doi.org/10.1002/mop.10975.

Cui, P., Zhang, A. M., Wang, S., & Khoo, B. C. (2018). Ice breaking by a collapsing bubble. *Journal of Fluid Mechanics, 841*, 287–309. https://doi.org/10.1017/jfm.2018.63.

Dular, M., Požar, T., Zevnik, J., & Petkovšek, R. (2019). High speed observation of damage created by a collapse of a single cavitation bubble. *Wear, 418–419*, 13–23. https://doi.org/10.1016/j.wear.2018.11.004.

Fortes-Patella, R., Challier, G., Reboud, J. L., & Archer, A. (2013). Energy balance in cavitation erosion: From bubble collapse to indentation of material surface. *Journal of Fluids Engineering, 135(1)*, 011303. https://doi.org/10.1115/1.4023076.

Fujikawa, S., & Akamatsu, T. (1980). Effects of the non-equilibrium condensation of vapor on the pressure wave produced by the collapse of a bubble in a liquid. *Journal of Fluid Mechanics, 97(3),* 481–512. http://doi.org/10.1017/S0022112080002662.

Goncalves da Silva, E., & Parnaudeau, P. (2021). Numerical study of pressure loads generated by a shock-induced bubble collapse. *Physics of Fluids, 33(11),* 1070-6631. https://doi.org/10.1063/5.0069332

Hammitt, F. G. (1963). Observations on cavitation damage in a flowing system. *Journal of Basic Engineering, 85(3),* 347–356. https://doi.org/10.1115/1.3656601.

Huang, G., Zhang, M., Ma, X., Chang, Q., Zheng, C., & Huang, B. (2020). Dynamic behavior of a single bubble between the free surface and rigid wall. *Ultrasonics Sonochemistry, 67,* 105147. https://doi.org/10.1016/j.ultsonch.2020.105147.

Huang, Y., Dai S. S., & Yuan, Z. M. (2024). Rapid validation of water wave metamaterials in a desktop-scale wave measurement system. *International Journal of Fluid Engineering, 1(1),* 013501. https://doi.org/10.1063/5.0191033.

Kornfeld, M., & Suvorov, L. (1944). On the destructive action of cavitation. *Journal of Applied Physics, 15(6),* 495–506. https://doi.org/10.1063/1.1707461.

Lauterborn, W., & Kurz, T. (2010). Physics of bubble oscillations. *Reports on Progress in Physics, 73(10),* 106501. https://doi.org/10.1088/0034-4885/73/10/106501.

Lechner, C., Koch, M., Lauterborn, W., & Mettin, R. (2017). Pressure and tension waves from bubble collapse near a solid boundary: A numerical approach. *Journal of the Acoustical Society of America, 142,* 3649–3659. https://doi.org/10.1121/1.5017619.

Luo, J., Xu, W.L., Deng, J., Zhai, Y., & Zhang, Q. (2018). Experimental study on the impact characteristics of cavitation bubble collapse on a wall. *Water, 10(9),* 1262. https://doi.org/10.3390/w10091262.

Ma, X., Huang, B., Zhao, X., Wang, Y., Chang, Q., Qiu, S., Fu, X., & Wang, G. (2018). Comparisons of spark-charge bubble dynamics near the elastic and rigid boundaries. *Ultrasonics Sonochemistry, 43,* 80–90. https://doi.org/10.1016/j.ultsonch.2018.01.005.

Matula, T. J., Hallaj, I. M., Cleveland, R. O., Crum, L. A., Moss, W. C., & Roy, R. A. (1998). The acoustic emissions from single-bubble sonoluminescence. *The Journal of the Acoustical Society of America, 103,* 1377–1382. https://doi.org/10.1121/1.421279.

Ohl, C. D., Kurz, T., Geisler, R., Lindau, O., & Lauterborn W. (1999). Bubble dynamics, shock waves and sonoluminescence. *Philosophical Transactions of the Royal Society A, 357(1751),* 269–294. https://doi.org/10.1098/rsta.1999.0327.

Ohl, C. D., Philipp, A., & Lauterborn, W. (1995). Cavitation bubble collapse studied at 20 million frames per second. *Annalen der Physik, 507(1),* 26–34. https://doi.org/10.1002/andp.19955070104.

Pecha, R., & Gompf, B. (2000). Microimplosions: Cavitation collapse and shock wave emission on a nanosecond time scale. *Physical Review Letters, 84,* 1328–1330. https://doi.org/10.1103/PhysRevLett.84.1328.

Plesset, M. S., & Prosperetti, A. (1977). Bubble dynamics and cavitation. *Annual Review of Fluid Mechanics, 9,* 145–185. https://doi.org/10.1146/annurev.fl.09.010177.001045.

Rayleigh, J. W. S. (1917). VIII. On the pressure developed in a liquid during the collapse of a spherical cavity. *The London, Edinburgh, and Dublin Philosophical Magazine and Journal of Science, 34(200),* 94. https://doi.org/10.1080/14786440808635681.

Supponen, O., Obreschkow, D., Kobel, P., Tinguely, M., Dorsaz, N., & Farhat, M. (2017). Shock waves from nonspherical cavitation bubbles. *Physical Review Fluids, 2,* 093601. https://doi.org/10.1103/PhysRevFluids.2.093601.

Tagawa, Y., & Peters, I. R. (2018). Bubble collapse and jet formation in corner geometries. *Physical Review Fluids, 3(8),* 081601. https://doi.org/10.1103/PhysRevFluids.3.081601.

Teslenko, V. S., (1980) Experimental investigation of bubble collapse at laser-induced breakdown in liquids. In: W. Lauterborn (eds.), *cavitation and inhomogeneities in underwater acoustics.* Springer Series in Electrophysics, vol 4. Springer, Berlin, Heidelberg., *4,* 3–34. https://doi.org/10.1007/978-3-642-51070-0_4.

Tomita, Y., & Shima, A. (1986). Mechanisms of impulsive pressure generation and damage pit formation by bubble collapse. *Journal of Fluid Mechanics, 169,* 535–564. https://doi.org/10.1017/S0022112086000745.

Trummler, T., Steffen J. S., & Nikolaus A. A. (2021). Effect of stand-off distance and spatial resolution on the pressure impact of near-wall vapor bubble collapses. *International Journal of Multiphase Flow, 141,* 0301-9322. https://doi.org/10.1016/j.ijmultiphaseflow.2021.103618.

Vogel, A., & Lauterborn, W. (1988). Time resolved particle image velocimetry. *Optics and Lasers in Engineering, 9(3–4),* 277-294. https://doi.org/10.1016/S0143-8166(98)90008-2.

Vogel, A., Lauterborn, W., & Timm, R. (1989). Optical and acoustic investigations of the dynamics of laser-produced cavitation bubbles near a solid boundary. *Journal of Fluid Mechanics, 206,* 299–338. https://doi.org/10.1017/s0022112089002314.

Yu, J. X., Luo, J. X., Li, Y. M. (2024). A review of bubble

collapsing near particles. *International Journal of Fluid Engineering*, *1(2)*, 020601. https://doi.org/10.1063/5.0193451.

Zhang, A. M., Wang, S. P., Bai, Z. H., & Huang, C. (2011). Experimental study on bubble pulse features under different circumstances. *Chinese Journal of Theoretical and Applied Mechanics*, *43(1)*, 71–83. http://doi.org/10.6052/0459-1879-2011-1-lxxb2010-278.

Zhang, G., & Zhang, H. T. (2024). Experimental studies of cavitation evolution through a butterfly valve at diferent regulation conditions. *Experiments in Fluids*, *65(4)*. https://doi.org/10.1007/s00348-023-03743-3.

Zhang, H. T., Wu, X., Lin, Z., & Zhang, G. (2024). Experimental study on cavitation inhibition in a butterfly valve with different plate shapes. *Physics of Fluids*, *36*, 023363. https://doi.org/10.1063/5.0187768.

Zhang, M., Chang, Q., Ma, X., Wang, G., & Huang, B. (2019). Physical investigation of the counterjet dynamics during the bubble rebound. *Ultrasonics Sonochemistry*, *58*, 104706. https://doi.org/10.1016/j.ultsonch.2019.104706.

Zhang, S., Wang, S. P., & Zhang, A. M. (2016). Experimental study on the interaction between bubble and free surface using a high-voltage spark generator. *Physics of Fluids*, *28*, 032109. https://doi.org/10.1063/1.4944349.

Zhu, H. J., Wang, Q., Mei, X. H., Wu, Y., & Zhao, C. (2022). A review on flow field velocimetry based on high-speed schlieren/shadowgraph systems. *Journal of Experiments in Fluid Mechanics*, *36(2)*, 49–73. https://doi.org/10.11729/syltlx20210110.